Review of Scientific Instruments

AIP Publishing

RESEARCH ARTICLE | APRIL 01 2024

Resonant inductive coupling network for human-sized magnetic particle imaging

Fabian Mohn ; Fynn Förger ; Florian Thieben ; Martin Möddel ; Ingo Schmale ; Tobias Knopp ; Matthias Graeser

Rev. Sci. Instrum. 95, 044701 (2024)
https://doi.org/10.1063/5.0192784

Review of Scientific Instruments ARTICLE pubs.aip.org/aip/rsi

Resonant inductive coupling network for human-sized magnetic particle imaging

Cite as: Rev. Sci. Instrum. 95, 044701 (2024); doi: 10.1063/5.0192784
Submitted: 20 December 2023 • Accepted: 7 March 2024 •
Published Online: 1 April 2024

Fabian Mohn,[1,2,a)] Fynn Förger,[1,2] Florian Thieben,[1,2] Martin Möddel,[1,2] Ingo Schmale,[3] Tobias Knopp,[1,2,4] and Matthias Graeser[4,5]

AFFILIATIONS

[1] Institute for Biomedical Imaging, Hamburg University of Technology, 21073 Hamburg, Germany
[2] Section for Biomedical Imaging, University Medical Center Hamburg-Eppendorf, 20251 Hamburg, Germany
[3] Philips GmbH Innovative Technologies, Research Laboratories, 22335 Hamburg, Germany
[4] Fraunhofer Research Institution for Individualized and Cell-based Medical Engineering, IMTE, 23562 Lübeck, Germany
[5] Institute of Medical Engineering, University of Lübeck, 23562 Lübeck, Germany

[a)] **Author to whom correspondence should be addressed:** fabian.mohn@tuhh.de

ABSTRACT

In magnetic particle imaging, a field-free region is maneuvered throughout the field of view using a time-varying magnetic field known as the drive-field. Human-sized systems operate the drive-field in the kHz range and generate it by utilizing strong currents that can rise to the kA range within a coil called the drive field generator. Matching and tuning between a power amplifier, a band-pass filter, and the drive-field generator is required. Here, for reasons of safety in future human scanners, a symmetrical topology and a transformer called an inductive coupling network are used. Our primary objectives are to achieve floating potentials to ensure patient safety while attaining high linearity and high gain for the resonant transformer. We present a novel systematic approach to the design of a loss-optimized resonant toroid with a D-shaped cross section, employing segmentation to adjust the inductance-to-resistance ratio while maintaining a constant quality factor. Simultaneously, we derive a specific matching condition for a symmetric transmit–receive circuit for magnetic particle imaging. The chosen setup filters the fundamental frequency and allows simultaneous signal transmission and reception. In addition, the decoupling of multiple drive field channels is discussed, and the primary side of the transformer is evaluated for maximum coupling and minimum stray field. Two prototypes were constructed, measured, decoupled, and compared to the derived theory and method-of-moment based simulations.

I. INTRODUCTION

Medical imaging modalities such as magnetic particle imaging (MPI) and magnetic resonance imaging (MRI) rely on alternating current to generate strong radio-frequency fields that form the backbone of signal generation and acquisition.[1,2] In the context of MPI, the frequency of the so called drive field does not depend on the Larmor precession of hydrogen atoms, nor is it correlated with a static B_0 field, as in MRI. The choice of this frequency is flexible, with the proviso that it should be above the human audible range but below frequencies where wave propagation effects begin to affect signal detection and below the limits for energy deployment due to the tissue's specific absorption rate (SAR).[3,4] Typically, this frequency falls in the range of 20–160 kHz,[3,5,6] where lower frequencies tend to cause more peripheral nerve stimulation (PNS).[7] In addition, the best non-linear signal response of the required magnetic nanoparticles (MNPs) that provide the image contrast in MPI falls into this range, depending on the particle's anisotropy.[8] Currents for a human torso system reach the kA range,[9,10] whereas head-sized systems require around 300–500 A.[11] While it is possible to perform MPI with non-sinusoidal excitation waveforms,[12,13] the benefit of using sinusoidal excitation lies in the ability to implement resonators such as passive filters. This study focuses primarily on MPI, while the basic concept has broader applicability to similar circuits and other frequencies. Such circuits can be found in the context of inductively coupled wireless power transmission,[14–17] power converters,[18,19] band-pass filters,[20–23] or other applications requiring high linearity and large currents. A prominent challenge in this context is the formulation of a resonant transformer, i.e., the primary side forms a resonance with the band-pass filter output stage, and the secondary side of the transformer is part of a high quality factor (Q) resonant transmit–receive circuit called the high current resonator (HCR).

Our purpose for the resonant transformer, referred to as the inductive coupling network (ICN), is to obtain a differential voltage system and a safe operating voltage. Ground loops and long, high-current cables can introduce undesired harmonics or disturbances into the received spectrum, i.e., induced by eddy currents in non-linear components such as unsoldered joints (screws). These distortions can dominate important particle harmonics, or sidebands, that are essential to the imaging process.[10,24] A differential design with balanced filters avoids a global ground node and is less susceptible to interference and noise.[25] Another strong advantage of a differential setup is floating signals with respect to the patient under examination, who is always capacitively coupled to the ground. A single-ended transmission chain entails the danger for humans if they come into contact with any single point in the system. As MPI systems strive for human trials,[6,11,26,27] this safety aspect cannot be ignored. Furthermore, reducing voltage levels in proximity to the patient requires a low inductance DFG, which in turn requires large currents to maintain the same field specifications.[9,11]

In this work, we design and implement a resonant toroidal inductive coupling network that encompasses safety concerns and incorporates a strictly linear and loss-optimized design. We elaborate on our design decisions and weigh different conditions and restrictions to present a new approach to finding suitable parameter choices, i.e., for inductors, cross section shape, parallel segments, gain, and dimensions. Our reasoning is intended to be transferable to other transformers under similar constraints using resonant loads for applications beyond medical imaging. Furthermore, we consider crosstalk by channel decoupling between multiple drive-field channels that each use an individual ICN and review multiple decoupling strategies. Based on a TxRx topology that was presented without details by Sattel *et al.*,[10] this study elaborates on the original implementation and optimization of an ICN and tailors the design parameters to a human-sized head scanner.[11]

II. MOTIVATION AND PURPOSE

Many current MPI systems use dedicated receive coils, often in a gradiometer configuration,[28–31] effectively suppressing feedthrough harmonics, interference, and systemic background.[24,32] However, receive coils take up valuable space and ultimately increase power consumption when signal generating coils have to be placed farther away, independent of the method of feedthrough suppression.[27] For preclinical systems with rodent-sized bores, power consumption can be managed; however, on the path to human-sized systems, this issue becomes a major challenge.[9,27] The advantage of choosing to combine the transmit and receive circuitry is that it reduces system complexity and overall space requirements by eliminating the need for a dedicated receive coil nested within the DFG and the receive band-stop filter.[33] One possible topology of a transmit–receive (TxRx) circuit is a symmetric HCR, as shown in Fig. 1(a), with a linear ICN, as shown in Fig. 1(b). A comprehensive characterization of the different noise and background contributions of TxRx and dedicated receive systems can be found in Ref. 24. However, there is currently no clear consensus in the community as to which system performs better on a human scale with manageable power consumption, although this may change in the future. The development of a TxRx system with an ICN is driven by various

29 April 2024 10:48:54

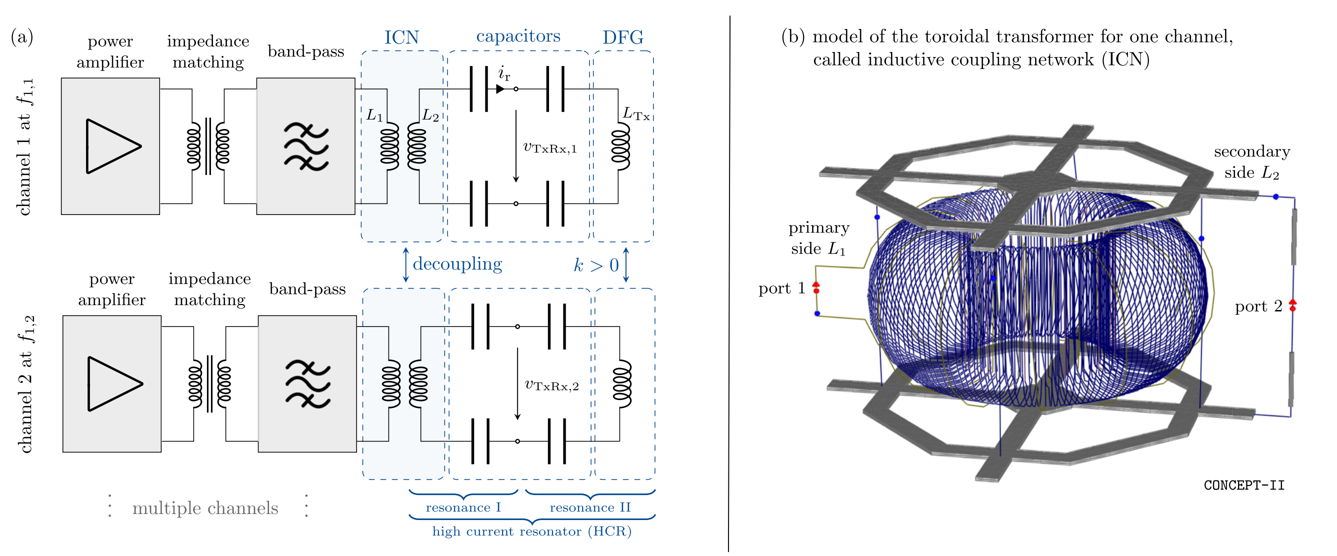

FIG. 1. Overview of the MPI transmit chain and the ICN. In (a), the power amplifier is connected to a ferrite-core transformer, a band-pass filter, and the primary side of the ICN. The secondary side of this transformer is part of a high-Q resonator, called a high current resonator (HCR), that includes the drive-field generator (DFG). Magnetic particles excited by the DFG induce signals via L_{Tx}, and the received signal is tapped within the symmetric HCR at v_{TxRx}. In (b), a four-fold segmented toroidal, D-shaped ICN is shown within a simulation setup of CONCEPT-II.[34]

design goals, including a. achieving floating potentials; b. ensuring linearity; c. attaining high current gain and high Q; d. designing circuit symmetry for excitation, filtering, and signal reception; and e. modularizing for impedance matching.

A. Floating potentials

The first design goal concerns patient safety and avoids ground loops that may negatively affect signal reception. A galvanically isolated high current resonator (HCR) with an overall low voltage and floating potential is achieved by many common transformer topologies. Floating potentials become relevant for a patient being examined in the scanner. Following the principle of the first fault case, the potential separation ensures that a patient is not exposed to a life-threatening current through single contact with the circuit. This would require contact at two separate points of the circuit, which drastically reduces the risk. In this unlikely event, we take the further precaution of reducing the overall voltage in the DFG and HCR by selecting low-inductance components.[11,35] A capacitive coupling network[36] would not provide real isolation at the drive-field frequency, although DC currents are blocked.

B. Linearity

A strictly linear air-core transformer is required because the ICN is located after the band-pass filter stage and must not increase the total harmonic distortion (THD) of the transmit or received signal. Harmonics generated directly within the HCR, where the received signal is tapped, would be unfiltered and, thus, mask and alter the particle's response. Harmonic generation by iron-core transformers is well known due to core saturation effects,[37,38] and the principle is demonstrated in Fig. 2(c). Here, we compare the THD after the band-pass filter with the THD generated by a ferrite-core transformer. Although an iron core would be preferable for its high permeability, effectively bundling magnetic field lines to achieve a high coupling coefficient k and low leakage inductance, it introduces distortion due to the saturation effects of the ferrite-core material. This constraint is so strong that a THD of 0.5% from a class-AB power amplifier in combination with our transmit filter results in a theoretical THD benchmark of below 5×10^{-6}%, calculated using the fundamental definition of $\mathrm{THD_F}$.[39] The typical THD of a linear power amplifier ranges from 0.1% to 1%,[40–43] and our filter achieves a measured 65 dB amplitude attenuation at the second harmonic f_2, 100 dB at f_3, and below 150 dB at f_4 and above.[11,23] Regarding a low-core loss iron powder material such as "−8" (Micrometals, Inc., CA, USA[44]) and neglecting any hysteresis effects, a maximum amplitude deflection of only 1% of the saturation field strength H_{sat} results in a THD of 3×10^{-3}%, as shown in Fig. 2(c-4). Although this number is extremely low, it is about three orders of magnitude higher than the combined THD of the amplifier and band-pass filter. Similarly, an amplitude of about $0.14 \times H_{\mathrm{sat}}$ would cause a THD of 0.5%, counteracting any achievements by the band-pass filter. Moreover, intermodulation of harmonics will occur, which further degrades the THD of an iron-core transformer, which was not modeled here. Consequently, an air-core transformer is preferred to achieve maximum linearity, and a toroidal shape is advantageous to enclose the majority of field lines within the toroid. This minimizes any coupling leakage flux and eddy current losses in the surrounding shielding and reduces the susceptibility to external disturbances to avoid spurious harmonics.

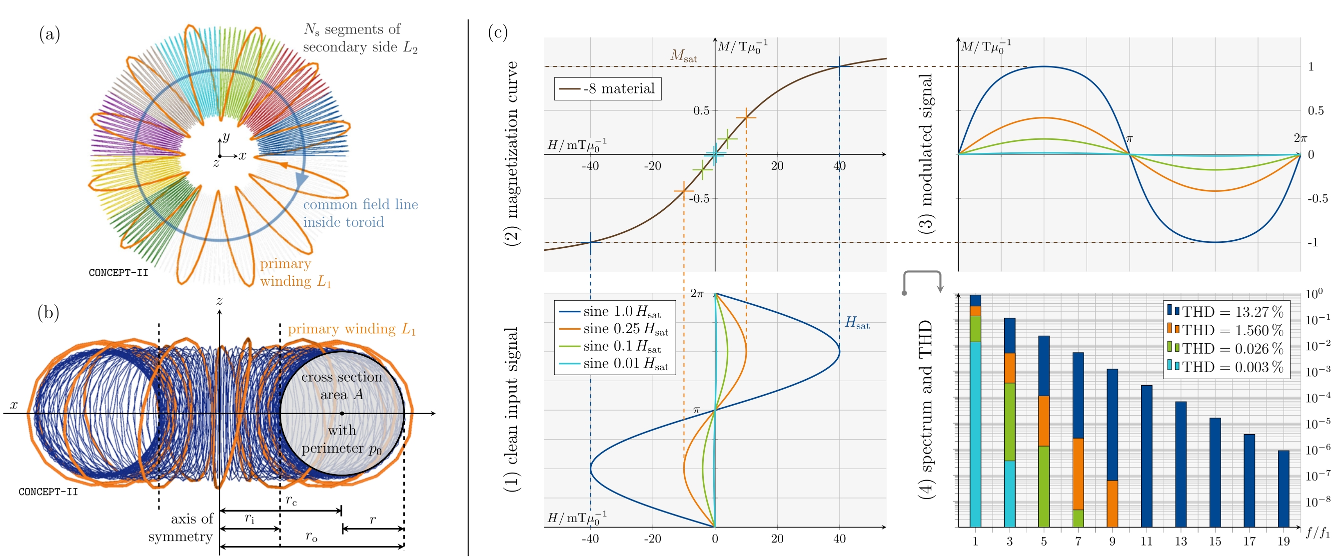

FIG. 2. Segmented toroidal air-core transformer and THD simulation of iron-core saturation without hysteresis. Shown in (a) is a toroid parallelized with $N_s = 12$ individual segments, of which eight are shown in different colors (four are hidden). The primary winding also forms a toroid, here with $N_1 = 12$ turns, whereas each secondary segment has $N_2 = 13$ turns. In (b), the circular cross section in the xz-plane is shown with characteristic parameters noted. On the right in (c), three sinusoidal input signals (1) are modulated by the magnetization curve in (2), which results in the output in (3) and its spectrum in (4). The magnetization curve is adapted from the "−8" iron powder core material,[44] but without hysteresis effects and modeled with a tanh-function.[45] A THD of 0.5%, typical for class-AB amplifiers, is caused by an amplitude of about 0.14 of H_{sat}.

C. High current gain and high Q

In order to maintain the same excitation field using low-inductance components, higher currents are required.[11] We are focusing on minimal conduction losses and an overall loss-optimized transformer design. The ICN is a resonant transformer, shown in Fig. 1(b), and the secondary side of the transformer is part of the HCR. Note that both voltage and current are amplified on the secondary side, unlike non-resonant transformers. This is based on a two-step process of having a tank LC with high impedance from the perspective of the primary side and the voltage scaling into a high Q load on the secondary side. However, amplification is due to resonance, and a change in the turns ratio still changes the voltage and current in opposite directions. A limiting factor in the gain is the structural size because it limits the overall achievable Q of the HCR.

Independent of the desired inductor values, the cross-sectional shape of the toroid is optimized to maximize the inductance L_2 for a given wire length, i.e., the perimeter p_0 of the toroidal cross section (D-shape). To achieve this, we implemented the results of a comprehensive study by Murgatroyd.[46] In addition, frequency dependent losses are minimized by using litz wires that suppress the skin effect and reduce proximity effect losses.[47] Due to the angular symmetry of the toroid, the winding core offers the possibility of parallel segmentation of the secondary side. Such parallel segments share the same enclosed field lines to compose a single composite toroid, as shown in Figs. 2(a) and 2(b), which can be used to shift the desired value for L_2 at a constant Q to change the desired turns ratio n. A trade-off must be made between wire diameter, feasible parallelization of toroidal segments, stacked wire layers near the symmetry axis, heat dissipation, and target inductance.

D. TxRx circuit symmetry

Symmetry refers to the HCR layout, where the capacitors are split into two separate banks for each inductor, as shown in Fig. 1(a). This offers the advantage of combining transmit and receive chains in a single circuit, as proposed by Sattel *et al.*[10] Here, the HCR acts simultaneously as a filter for the fundamental frequency, allowing it to tap the particle's response v_{TxRx} during transmission. However, a partial attenuation of the particle signal is inevitable using this configuration because the strength of the particle signal relies on the proportion of inductors L_2 and L_{Tx}, which we call the DFG matching condition.

E. Impedance matching modularization

For feasible impedance matching, a modularization into two matching stages is carried out, as shown in Fig. 1. The ICN can thus be designed without additional constraints regarding amplifier load matching, which is done separately by an amplifier matching stage. To this end, we use a ferrite-core transformer before the band-pass filter with a maximum amplitude below 10% of H_{sat}, as explained in Sec. II B, on the condition that the transformer's THD is similar to the amplifier's THD and a band-pass filter is implemented afterward.

III. THEORY

In this section, we present a systematic optimization of an inductive coupling network, delineating the theory and criteria employed to derive the configurations for both sides of the toroidal transformer. Our approach commences with an examination of the transformer's current gain G in Secs. III A and III B. The focus then shifts to optimizing the toroidal geometry with the goal of minimizing losses and maximizing inductance, as described in Sec. III C. This optimization process encompasses cross-sectional shape, multiple winding layers, segmentation, and primary winding characteristics. In order to select an appropriate inductance value, we proceed to the inductance matching condition specific to a symmetric setup of the HCR in Sec. III D, a consideration tailored for the MPI imaging modality.

Given the broader context of multichannel MPI systems, it is imperative to devise individualized ICNs for each channel and account for coupling, which is described in Sec. III E. Nevertheless, up to that point, the entire section focuses on a single channel with the resonance frequency f_1.

A. Maximum transformer current gain

The current amplification factor, denoted as G for the ICN transformer, will be investigated with the objective of maximizing it, according to design goal c. A first expression for G can be derived by considering the power P_2 on the secondary side, caused by the primary current i_1 that induces the voltage v_2, as in

$$P_2 = \frac{|v_2|^2}{R_{\mathrm{s}}} = \frac{|j\omega M i_1|^2}{R_{\mathrm{s}}} = \frac{\omega^2 M^2 |i_1|^2}{R_{\mathrm{s}}}, \tag{1}$$

where $\omega = 2\pi f_1$ denotes the channel angular frequency, j denotes the imaginary unit, M denotes the mutual inductance of the transformer, and $R_{\mathrm{s}} = R_2 + R_{\mathrm{Tx}}$ denotes the total series resistance of the secondary side at resonance (capacitor losses are neglected).[48] All components, currents, and voltages are shown in Fig. 3. Now, the power at resonance can be rewritten to obtain the current gain G by

$$|i_2|^2 R_{\mathrm{s}} = \frac{\omega^2 M^2 |i_1|^2}{R_{\mathrm{s}}} \quad \Rightarrow \quad G = \frac{i_2}{i_1} = \frac{\omega M}{R_{\mathrm{s}}}. \tag{2}$$

In the following, this expression is rearranged for resonant transformers using characteristic transformer variables such as the turns ratio n, the coupling coefficient $k \in [0, 1]$, and the quality factor Q of the transformer's secondary side.[49,50] Note that voltages across the leakage inductance $L_{\sigma,1} = L_1(1-k)$ and matching capacitor C_{m} of

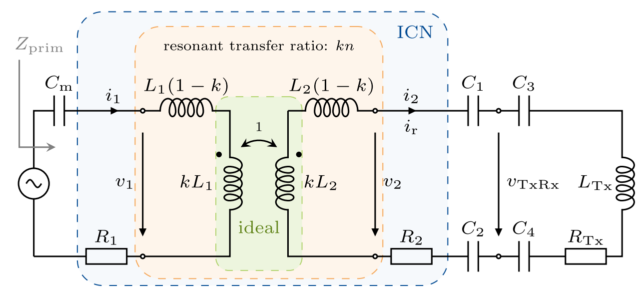

FIG. 3. Resonant transformer circuit diagram. A resonant transformer is shown, where an ideal transformer remains embedded in the center. The inductors are split into leakage and coupled inductances. The matching capacitor C_{m} resembles the filter output stage, which goes into resonance with the leakage inductance $L_{\sigma,1} = L_1(1-k)$, and Z_{prim} becomes real at $\omega = 2\pi f_1$.

the band-pass filter cancel at resonance. Furthermore, L_2 is part of a resonant circuit on the secondary side; therefore, voltage and current are increased.

The turns ratio is defined by the number of primary turns N_1 to secondary turns N_2. For an ideal transformer that is perfectly coupled ($k = 1$), there is no phase difference and, therefore, no losses between the two sides. In this case, n directly relates the magnitude of the voltages v_1 and v_2 and can be used to step up or step down the reflected impedance seen at the input,[50] as given in

$$n = \frac{N_1}{N_2} = \sqrt{\frac{L_1}{L_2}} = \frac{v_1}{v_2}. \tag{3}$$

L_1 and L_2 are the transformer's primary and secondary inductances. Next, to obtain the coupling coefficient, we first consider the coupling factors,

$$K_1 = \frac{\Phi_{21}}{\Phi_{11}} = \frac{M}{L_1}, \quad K_2 = \frac{\Phi_{12}}{\Phi_{22}} = \frac{M}{L_2} \tag{4}$$

for the general case of arbitrary transformer shapes. K_1 measures the proportion of the mutual magnetic flux Φ_{21} caused by a current i_1 in M and the magnetic flux Φ_{11} caused by a current i_1 in L_1. The same principle applies to K_2. Note that the value of K_i can be greater than 1. The mutual inductance M is reciprocal for all linear materials with symmetric tensors for electric conductivity, permittivity, and permeability.[51] Now, the definition of the coupling coefficient is given with

$$k = \frac{M}{\sqrt{L_1 L_2}} = \sqrt{K_1 K_2}. \tag{5}$$

Finally, a general expression for the quality factor Q is given by the ratio of stored energy to dissipated energy per cycle: For an inductor L, perfect capacitors, and assuming negligible radiation losses in the kHz region, the quality factor is

$$Q = 2\pi \frac{E_{\text{stored}}}{\frac{1}{f} P_{\text{diss}}} = 2\pi f \frac{\int_0^{\hat{i}} L\, i\, \mathrm{d}i}{\left(\frac{\hat{i}}{\sqrt{2}}\right)^2 R} = \frac{\omega L}{R}. \tag{6}$$

R is the total resistance of the considered resonance,[52] and $\hat{i}$ is the total current of the inductor.

Under the consideration of a dominant Q of the coils, the three constituents of the gain in (2) are replaced by the considered ICN, and the equation yields

$$G = \frac{\omega M}{R_s} = \frac{\omega L_2}{R_s} \frac{M}{\sqrt{L_1 L_2}} \sqrt{\frac{L_1}{L_2}} = Q\, k\, n. \tag{7}$$

Note that the inserted Q refers to the transformer with its energy stores L_2, C_1, and C_2, while the resonance on the right side acts as a real impedance, adding only the serial resistance R_{Tx} of the DFG.

There are three conclusions due to (7): The channel frequency should be chosen as high as reasonable, taking into account the drawback of increasing losses due to high-frequency effects in the transmit and receive chains. We consider fixed frequencies in the low kHz range (around 26 kHz) and discuss the frequency choice in Sec. VI. Second, a reduction of R_s is beneficial: The correct type of litz wire should be chosen,[47] connections within the HCR should be kept short, and the cross section shape of the inductor should be chosen to obtain a minimum R for a maximum L[46,53] to result in a high Q. Apart from minimizing R, the goal of maximizing M requires finding a toroid with both a high k and a large L. A high turns ratio n can be obtained by a dense primary winding and parallelizing the second transformer side. Third, as the total energy dissipated must equal the energy delivered in the resonant circuit, we obtain

$$|P_1|\Delta t = |P_2|\Delta t \quad \Rightarrow \quad \mathrm{Re}(Z_1) = G^2\, \mathrm{Re}(Z_2) \tag{8}$$

for a time interval Δt at steady-state, $Z_1 = v_1/i_1$ and $Z_2 = v_2/i_2$. The imaginary part is zero at resonance, and the real impedance seen by the primary side equals

$$\mathrm{Re}(Z_{\text{prim}}) = R_1 + G^2 R_s = R_1 + \frac{\omega^2 M^2}{R_s}. \tag{9}$$

B. Structural size limits Q

As argued above and evident from Eq. (7), we need a large secondary inductance to obtain a high transformer gain. A large structural size is beneficial because an increasing cross section A increases the inductance faster than its reduction by the growing center radius r_c, as approximated by the equation for a single-layer air-core toroid with a circular cross section,

$$L_{\text{toroid}} \approx \frac{\mu_0 N^2 A}{2\pi r_c}. \tag{10}$$

Here, μ_0 is the vacuum permeability, and the dimensions are shown in Fig. 2(b). However, a constant number of turns that are stretched around a growing cross section will reach a point where the changes in inductance and resistance compensate. This problem and its parameter dependencies are a well-known optimization problem, treated by Murgatroyd,[46,53] and an overview can be found in Ref. 54. A can be increased until an optimum is reached where the inductance is maximum for a given total wire length $l = N 2\pi r$ of all turns. This is a restraint on A, and there exists an optimum for the ratio of outer to inner radius for a finite l. The optimum number of turns for toroids with a circular cross section and wire diameter d lies at $N = 0.8165\sqrt{l/d}$, which in turn yields the ratio $r/r_i = (0.8165)^{-2} \approx 1.5$ and the optimal inductance,

$$L_{\text{toroid,opt,circ}} \approx \frac{\mu_0\, d}{2\pi}\left(0.2722\left(\frac{l}{d}\right)^{\frac{3}{2}} + 0.25\frac{l}{d}\right), \tag{11}$$

as derived by Murgatroyd.[54]

Optimal benefits are obtained from the correct area to radius ratio in combination with a large overall construction volume, coupled with a judicious selection of layers within the interior, as shown in Fig. 4(b) and explained in Sec. III C 2. The upper limit is reached if the interior space is fully occupied by wires, which also affects the cross section shape that deviates from a circle for the outer layers.[53,55] Overall, increasing the dimensions of the toroid leads to an increase in L_2, Q, and, thus, G. The maximum Q is defined by the available construction volume.

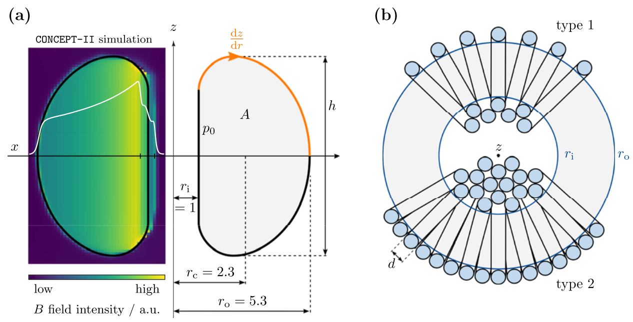

FIG. 4. Optimal D-shaped cross section and multi-layer toroids.[53] In (a), the optimal D-shape cross section is shown for the fixed optimum ratio of $r_o/r_i = 5.3$. The left toroid-half features a field intensity plot with the field profile along the x-axis in white (the toroid has three layers on the inside, simulated in CONCEPT-II[34]). Highlighted in orange in the right toroid-half is the curve obtained by a stepwise evaluation and integration of (13). In (b), two different types of winding arrangements of multi-layer toroidal inductors are shown.

C. Toroidal transformer

The ICN toroid is optimized for a finite available construction volume by optimizing the cross-sectional shape for a higher inductance, taking into account multiple layers of winding, and improving the coupling of the primary winding. Then, segmentation provides a tuning mechanism that allows us to change the nominal inductance with a constant inductance-to-resistance ratio[56] to a desired value.

1. Optimal cross section: D-shape

A circular cross section gives the largest area A for a fixed turn perimeter p_0, but it does not provide the highest inductance for this wire length. This discrepancy is caused by the non-uniform flux density within A, which is denser toward the inside for toroids,[54,57] as shown in Fig. 4(a). Due to the straight inner edge of the D-shape, it encompasses the higher magnetic flux density toward the z-axis of symmetry and yields ~15% more inductance than the circular window for the same p_0.[54]

For the single-layer DC loss optimized D-shape, the optimum was found to be

$$L_{\text{toroid,opt,D}} \approx \frac{\mu_0\, d}{2\pi}\left(0.314\left(\frac{l}{d}\right)^{\frac{3}{2}} + 0.25\,\frac{l}{d}\right) \tag{12}$$

for $\frac{r_o}{r_i} = 5.3$ and $N = 0.565\sqrt{\frac{l}{d}}$,[53] as shown in Fig. 4(a). The slope (orange) is obtained by a stepwise evaluation along the radial direction, given by

$$\frac{\mathrm{d}z}{\mathrm{d}r} = \pm\frac{\ln\frac{\sqrt{r_i r_o}}{r}}{\sqrt{\ln\frac{r}{r_i}\ln\frac{r_o}{r}}}. \tag{13}$$

Integrating the slope $\mathrm{d}z/\mathrm{d}r$ yields coordinates for the optimized quarter section shapes.

AC losses are mainly eddy current losses due to proximity effects, since the skin effect plays only a minor role in litz wire windings. The impact of the proximity effect is twofold: internal magnetic fields due to neighboring currents cause eddy currents, but they are dominated by the second effect due to the main toroidal field through the rest of the coil, acting on the entire litz wire bundle.[47] Overall, this results in eddy currents causing local non-uniform current densities that require a more complex shape optimization for high frequencies, as can be found in Ref. 46. The optimum shape for high frequencies differs from a D-shape due to the stronger constraint of eddy current losses, which are highest near the center, causing the highest point of the slope to move outward. However, in the kHz range, the AC optimized shape converges to the DC optimized shape of (13) for litz wires with sufficiently small strands.

2. Multiple layers

Another way to effectively increase L_2, which optimizes Q, is by using multiple wire layers. However, insufficient heat dissipation from the inner layers becomes an issue that, in turn, increases copper resistance and might damage the litz wire insulation layer. To this end, we propose a single, nearly dense outer layer of turns, as shown in Fig. 4(b), which overlap on the inside near the axis of symmetry. This compromise gives satisfactory results and sufficient heat dissipation by air cooling. If the litz wire winding is not operated near its maximum current rating, e.g., for split-core toroids in filter stages,[11,23] multiple dense layers are an efficient option. A general study on optimal shapes for air cores and non-air core multilayered toroidal inductors can be found in Ref. 55.

3. Segmentation

The secondary side L_2 can be divided into N_s identical segments, which are wired in parallel but enclose a single common field, as shown in Figs. 2(a) and 2(b). If the winding remains otherwise unchanged, both the inductance and the resistance will be reduced with N_s^2 if N_s is increased. As an example, a segmentation into two halves is considered, where one half is limited to $N/N_s = N/2$ turns. Intuitively, it seems that L is reduced quadratically and the resistance R is reduced linearly for a dense winding that remains unchanged, due to $L \propto N^2$ via (10) and $R \propto N$ via each turn perimeter. However, the effect for L is changed to $L \propto N$ due to the shorter magnetic core length l, exemplified by a long and straight solenoid with $L \propto N^2/l \propto N$ that has a constant turn density N/l. An additional slight decrease in L is caused by the now open magnetic circuit, which results in less coupling of the end turns with the rest of the toroid. Mutual coupling M compensates for this loss of self-inductance L for toroids since the halves now couple to the parallelized second half, i.e., to their neighbors at both ends if again arranged as a joint toroid after segmentation. However, parallelizing equal impedances results in a $1/N_s$ division for both L and R. Overall, the linear contribution of the separation and the linear contribution of the parallelization result in a $1/N_s^2$ scaling for both L and R.

A segmented toroid with $N_s = 12$ segments is shown in Fig. 2(a), and the total current is distributed by a central node (copper plates) at the top and bottom. A lead wire from each segment is connected to the node as shown in Fig. 1(b) for $N_s = 4$. Another aspect of the segmentation is that the current i_r of the HCR is divided equally among the parallel segments, thus relaxing the copper cross section requirements for the L_2 winding. In system design situations, the construction volume is usually constrained to a maximum bounding box. For an optimal shape, Q is thus fixed. Using this method, the design can start with an optimal single winding inductor and then use segmentation to tune for a desired L_2 and R_2.

4. Primary winding

A final design decision for the toroidal topology concerns the primary winding. For a reasonable volume and, therefore, limited Q, the primary winding should achieve a high coupling k, as shown in (7). Consequently, one choice is that L_1 is also toroidal and (sparsely) wound around the outside of L_2. This ensures that the majority of the field lines are shared by both transformer sides to maximize k. In Fig. 2(b), such a toroidal primary winding of L_1 (orange) is shown for a toroid with a circular cross section. Known from Rogowski coils[58] is the beneficial effect of a return wire in the xy-plane that counteracts the single turn of l along the center circumference of the toroid to diminish the field on the outside, which is in line with the z-axis. For ease of fabrication, we propose a return wire along the outside at r_o, which suppresses most of the stray field but deviates from the optimal enclosed position at r_c.

If a dense L_1 coil is used, i.e., a few turns at one point around the toroid, the result is a large K_1 and a very weak K_2. The overall k is small, which is only sufficient for a design with a very large Q. However, such a dense L_1 provides several advantages for peripheral measures, such as a pick-up coil to measure the current, i_r. Such a coil, L_3, could be mounted on the toroid opposite to L_1 to focus its sensitivity locally on L_2 and avoid coupling between L_1 and L_3.

D. DFG matching condition

We have previously shown that, in order to achieve high gain for design goal c, it is advantageous to obtain a high Q. Currently, the inductance of L_2 itself is not considered. In the following, a trade-off is identified that characterizes L_2 in its dependence on L_{Tx} to comply with design goal d. This consideration arises from the specific constraints imposed by the MPI imaging setup, in particular the circuit symmetry condition for simultaneous transmission and reception and the absolute power consumption, which has not been considered so far. Here, we assume a constant Q, which is justified for a fixed bounding box as reasoned in Sec. III B, resulting in a linear relationship between R_2 and L_2 at a fixed ω. The ohmic resistances of the capacitors and the DFG remain constant.

Our objectives are twofold, yet inherently contradictory: achieving both maximal particle signal strength at the v_{TxRx} port and minimal power consumption within the HCR. The particle response is characterized by the prevalence of high-order harmonics at the resonance frequency f_1. These harmonics experience a significant voltage drop across an inductive voltage divider formed by the inductances L_2 and L_{Tx} when compared to the relatively minor influences of their small series resistances within the mΩ range[11] and the associated HCR capacitors at harmonic frequencies. The winding configuration of L_{Tx} can be conceptualized as a distributed voltage source, thereby inducing the particle voltage at the virtual ground nodes of v_{TxRx}.[10] Ideally, in the scenario of an infinitely large L_2, the complete induced voltage would be dropped across L_2, leading to a maximal particle response at v_{TxRx}. In contrast, a diminished ratio of L_2/L_{Tx} would effectively short-circuit the receive voltage, advocating a maximum value for L_2. However, the cumulative series resistance $R_2 \propto N2\pi r$ of the toroid manifests the same increase as L_2 is augmented, as imposed by a constant Q via (6). The total power consumption increases with R_2, but it is limited to a feasible amount. This imposes a constraint on L_2 because the current amplitude at resonance i_r in the HCR must stay constant to maintain the same

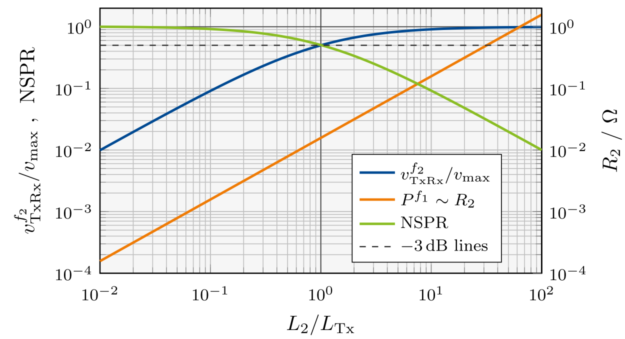

FIG. 5. Inductance matching condition of DFG and ICN. A trade-off is identified at $L_2 = L_{Tx}$ when the received signal is halved (−3 dB), expressed by the intersection of the particle signal (blue) and the normalized signal-to-loss ratio (green). This graph demonstrates that additional power is required to avoid receiving signal attenuation.

drive field strength. Consequently, a partial attenuation of the particle signal is inevitable due to the voltage division effect inherent in the inductance voltage divider of L_2 and L_{Tx}.

The crucial point is that the power consumption at the fundamental f_1 scales linearly with R_2, and the particle voltage at frequencies $f > f_1$ drops depending on the inductive voltage divider when the impedance of capacitors becomes negligible. We consider a unit current $i_r = 1$ A and define the particle signal-to-power ratio (SPR) as

$$\mathrm{SPR} = \frac{v^{f_2}_{TxRx}}{P^{f_1}} = \frac{v^{f_2}_{TxRx}}{i_r^2 R_2}. \tag{14}$$

The power consumption P^{f_1} is considered at the fundamental, but the particle signal $v^{f_2}_{TxRx}$ is at the first harmonic. Note that for f_2 and all higher frequencies, the inductive voltage divider is the dominant part, and all harmonics are recorded. The maximum particle voltage v_{max} of $v^{f_2}_{TxRx}$ is defined in the limit of a large L_2, where it is not attenuated. To remove the influence of the absolute value of R_2, we normalize (14) with its maximum in the parameter range and call it NSPR. The constituents of (14) and the NSPR are plotted in Fig. 5.

One possible trade-off position can be identified at −3 dB of NSPR and $v^{f_2}_{TxRx}$, which results in halving the received signal (harmonics). This point coincides with $L_2 = L_{Tx}$, where the inductances match, which we chose as the trade-off for the design of our ICNs. Consequently, a less attenuated particle signal requires more power. Note that (14) remains valid when L_{Tx} is varied instead of L_2, and the consideration of the inductance voltage divider remains identical.

E. Channel decoupling

The use of multiple channels in MPI has the advantage of simultaneous sampling of a 3D field-of-view (FOV). Due to the imperfect spatial orthogonality of these channels and the close proximity of resonance frequencies, typically within a range of less than $\Delta f = 0.03 f_1$,[59] strong coupling between the different drive-field channels is expected. Thus, even weak coupling coefficients present a particular challenge, especially in the case of resonant circuits with high Q, necessitating the development of effective decoupling mechanisms while introducing minimal additional resistance to the HCR.

Causes of channel coupling are misalignment of the drive-field coils, non-orthogonal field components, and undesired loops in the connecting wires. Small errors in positioning, e.g., for two planar coils with $k \propto \cos(\beta)$, can lead to coupling with significant currents. A $\beta = 3^\circ$ results in $k = 0.052$, which can generate a current $i_{r,2}$ in channel 2 of similar magnitude to the original current $i_{r,1}$ in channel 1. For this purpose, if we consider the complex impedance $Z_{HCR,2}$ of the second channel's HCR and let j be the imaginary unit, then the current $i_{r,2}$ in the second channel at the first angular frequency $\omega_{r,1}$ is caused by induction via $i_{r,1}$ and M, as in

$$\begin{aligned}\frac{i_{r,2}(\omega_{r,1})}{i_{r,1}(\omega_{r,1})} &= \frac{v_{ind,21}(\omega_{r,1})}{Z_{HCR,2}(\omega_{r,1})}\frac{1}{i_{r,1}(\omega_{r,1})}\\ &= \frac{j\omega_{r,1}M\, i_{r,1}(\omega_{r,1})}{Z_{HCR,2}(\Delta\omega+\omega_{r,2})\, i_{r,1}(\omega_{r,1})}\\ &\approx \frac{j\omega_{r,1}M}{j2\Delta\omega(L_{Tx,2}+L_{2,2})} \approx \frac{\omega_{r,1}M}{4\Delta\omega L_{2,2}} = \frac{1}{4}\frac{\omega_{r,1}}{\Delta\omega}k. \qquad (15)\end{aligned}$$

Note that the matching criterion of Sec. III D is respected with $L_{Tx,2} = L_{2,2}$, and we approximate $Z_{HCR,2}$ near $\omega_{r,2}$ with $j2\Delta\omega L_{2,2}$, as shown in Appendix A 1. With $\frac{\Delta\omega}{\omega_{r,1}} = \frac{(\omega_{r,1}-\omega_{r,2})}{\omega_{r,1}} = \frac{1}{75}$ (see the beginning of Sec. V) and the aforementioned misalignment of $\beta = 3^\circ$, this example results in $\frac{i_{r,2}}{i_{r,1}} = 0.25 \cdot 75 \cdot 0.052 = 0.975 \approx 1$. The consequence is a severe distortion of the Lissajous trajectory, which is already significant for values $i_{r,2}/i_{r,1} \geq 10\%$.[60]

In order to avoid the negative effects of uncompensated couplings, such as trajectory distortion, additional power dissipation, detuning, and frequency beating that will act on the power amplifier, we consider three types of decoupling schemes: capacitive, inductive, and active compensation. Capacitive compensation is narrowband and requires additional connections between channels, but the equivalent series resistance (ESR) of capacitors is low. Inductive compensation is directed at counteracting M and is broad-band, but additional coils typically increase the series resistance, thus reducing Q. Finally, active decoupling uses the channel's amplifiers but demands reactive power in the band-pass filters [Fig. 1(a)] and for the mismatched HCR. Furthermore, it requires accurate feedback for current control. It should be considered a last resort, as the amplifier will see a reactive load at other frequencies, and maximum voltage ratings may be exceeded over the course of a full Lissajous trajectory cycle.

In general, capacitive decoupling may not offer an exact solution, and there are unsolvable combinations of coupling depending on the sign of the coupling coefficients. However, capacitive compensation is advantageous for the particle signal of a transmit–receive circuit because a large common series capacitor can be used, which becomes short at harmonic frequencies and has a very low series resistance compared to coil windings. This requires two common nodes between channels and similar inductive coupling coefficients of the same sign, due to the single narrowband decoupling point. We could use three capacitors, two within each channel, or, alternatively, one common capacitor for all channels. The mentioned low differences in drive-field frequencies in MPI are a premise, and a limitation is that the sum of all currents flows through this capacitor. A schematic is shown in Fig. 6(a), which represents only the right part of the symmetric HCR, with v_{TxRx} across each numbered a-b terminal pair, shown for three channels each.

Inductive compensation is a general alternative for all coupling coefficient signs. Either a coil is added in series to L_{Tx} for each unique off-diagonal entry of the system's impedance matrix, as shown in Fig. 6(b), or the same number of separate windings is used to introduce the desired compensation without a galvanic connection by careful positioning, as shown in Fig. 6(c). A disadvantage of the first technique is the additional high current lines, stray fields, their influence on the tuning of the resonators, and additional series resistance, as well as their mounting and cooling effort. The second technique uses separate windings that are sensitive to a partial amount of the drive-field, equal to the M introduced by coupling. A suitable

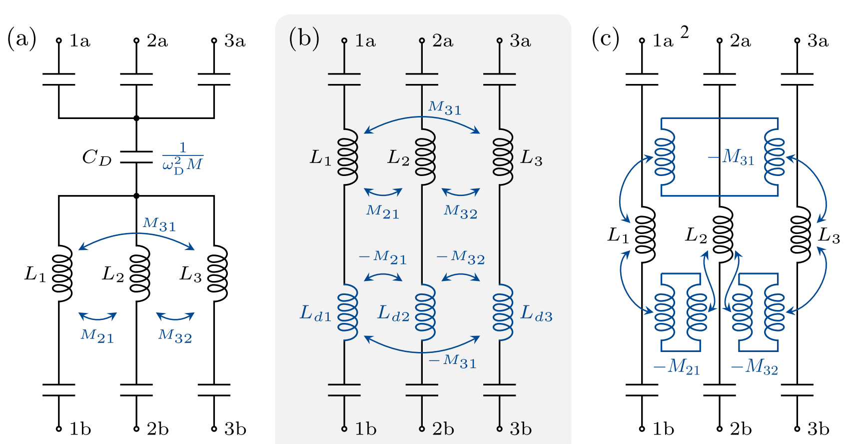

FIG. 6. Schematic of decoupling schemes with three TxRx channels. The schematics refer to one-half of the symmetric HCR, where v_{TxRx} can be tapped across each numbered a–b terminal pair (compare Fig. 1). Capacitive decoupling for a single frequency via a common capacitor C_D is shown in (a), with the condition that $M_{21} \approx M_{32} \approx M_{31}$. Inductive decoupling strategies (broadband) are shown in (b) and (c), for the case of series inductors and the case of separate windings, respectively.

inductive decoupling position is the ICN itself, as implied in the last paragraph of Sec. III C 4. Turns on the outer surface of the toroid are only capable of utilizing integer multiples to achieve a match with M. However, a slab outfitted with a wire loop can be introduced to encompass a partial quantity of the magnetic field inside: a loop on a slab that is inserted into a prepared gap within the toroid. Adjustment of the slabs can be used to fine-tune each channel if the ICN was prepared with such gaps. The sign can be adapted by inverting the orientation of the wire-loop. However, the principle remains the same if it is done with partial fields in the proximity of the DFG.

For our two-channel human-sized system,[11] we decided to use a single common capacitor that carries a peak current of $i_{r,1} + i_{r,2}$ (depending on the phase of the Lissajous cycle), introducing the same voltage as M into each circuit but with the opposite sign. The common decoupling capacitor C_D is calculated at a single frequency ω_D in-between both drive-field frequencies by

$$C_D = \frac{1}{\omega_D^2 M} = \frac{1}{(\pi(f_{r,2} + f_{r,1}))^2\, k\sqrt{L_{Tx,1}L_{Tx,2}}}. \tag{16}$$

This narrowband solution is acceptable for our implemented two-channel system, and the additional ESR introduced by the decoupling capacitor is small.

IV. METHODS AND IMPLEMENTATION

Guided by the theory to optimize the ICN for a given bounding box, we now describe the implementation and name the changes to our design that deviate from the stated optimum. We employ simulations to assess performance in Sec. IV A, which includes a D-shaped toroid. They are used to refine our decision on the number of segments and the type of primary winding. The construction of two ICNs is described in Sec. IV B, and the measurement methodology to analyze the prototypes is given in Sec. IV C.

A. Simulations

Linear circuit simulations are performed with LTspice 17.1 (Analog Devices, MA, USA).[61] Simulations of the magnetic field and the transformer's impedance matrix are performed using CONCEPT-II (Institut für Theoretische Elektrotechnik, Hamburg University of Technology, Germany).[34]

1. Toroid geometry

The CONCEPT-II software is based on the method of moments (MoMs) that solves electromagnetic boundary or volume integral equations in the frequency domain.[62] It is especially suited for the numerical computation of 3D radiation and scattering problems. CONCEPT-II is used in our work to calculate and test different toroidal transformer configurations. Input parameters include the general geometry (distances, shape and size of A, number of segments N_s, turns N_1 and N_2, primary winding shape, number of overlapping layers inside the toroid), while important output parameters include the impedance matrix $\boldsymbol{Z}$, 3D field plots, and conductor current densities. A two-port network is used to estimate k and G via the impedance matrix of the transformer,

$$\boldsymbol{Z} = \begin{bmatrix} Z_{11} & Z_{12} \\ Z_{21} & Z_{22} \end{bmatrix} \approx \begin{bmatrix} R_1 + j\omega L_1 & j\omega M \\ j\omega M & R_2 + j\omega L_2 \end{bmatrix}. \tag{17}$$

Different numbers of segments N_s are simulated, as well as the coupling between neighboring segments. Stray fields are minimized and coupling is maximized by looking at different winding options for L_1 (dense vs sparse/distributed), the suited number of turns N_1, and the current density in the copper-plates where parallel segments are joined. Litz wire windings are approximated by a single thin wire, assuming that the currents are restricted to the direction of the wire and the copper conductivity of surfaces and wires is set to $\sigma = 58 \times 10^6$ S m^{-1}. The results of the simulation are used to adapt the design and finally to compare the expectations with the manufactured prototypes in terms of L, k, n, and G. One simulated B-field plot is shown in Fig. 4(a) for a number of three overlapping wire layers on the inside. One complete model (four segments) is shown within the simulation framework in Fig. 1(b), including copper distribution plates.

2. Circuit analysis

With simulated values for L_1, L_2, k, and resistors as input parameters, the resonance behavior is analyzed in the schematic circuit analyzer tool LTspice. A model of the entire HCR is simulated, including the band-pass filter stage, the ICN, and two channels including crosstalk. Different decoupling strategies are tested to probe the schematic, based on Fig. 3, and to tune values for decoupling elements. The input impedance value, Z_{prim}, was also simulated with LTspice. A simplified LTspice model without the band-pass is provided in the supplements with two coupled channels, including the HCR, and approximate values for capacitors and inductors.

B. Construction of two toroidal ICNs

To weigh the different design decisions of the ICN, we followed the reasoning of Secs. III and IV A consecutively. The construction was performed after the simulation, with the probed values for parameters L, N, the number of segments $N_{s,1} = 4$ and $N_{s,2} = 6$, as given in Table I, and the chosen dimensions of $r_i = 4$ cm, $r_o = 9.2$ cm, and the height $h = 8.6$ cm for the D-shaped second side. Moreover, we use the channel frequencies $f_{1,1} = 25.699$ kHz and $f_{1,2} = 26.042$ kHz with a distance of $\Delta f = 343$ Hz.

The choice of $N_s = 6$ segments for the second channel is owed to the fact that we implemented a saddle coil (DFG of channel 2), which requires a higher current than the first channel to meet field specifications;[11] thus, we chose to reduce R_2. Due to the fact that Q remains constant, the increase in gain is caused by the turns ratio n due to the shift in the ratio of L_1 to L_2. As reasoned in Sec. III C 3, the inductance decreases for a higher number of segments, which also better fits the lower DFG inductance of the saddle coil to comply with the matching condition of Sec. III D. To further increase the turns ratio n of the second channel, we chose $N_{1,2} = 13$ instead of $N_{1,1} = 12$. As a consequence, we were able to use the same support structure for winding, and both ICNs are of equal dimensions despite their different objectives. The 3D printed toroidal support structure of the ICN is made from the high temperature resin RS-F2-HTAM-02 (Formlabs, MA, USA). Air cooling along the symmetry axis is installed using shielded fans to prevent impedance changes caused by insufficient heat dissipation.

A difference between the derived optimal design and the constructed ICNs is the ratio of radii $r_i/r_o = 2.3$ for the D-shaped toroid.

TABLE I. Values from simulation (yellow) and measurement (blue) for both constructed ICNs. Bold fonts denote important values.

			L / μH	R / mΩ	N	f_1 / Hz	M / μH	Q_{ICN}	Q_{HCR}	n	k	G	Z_{prim} / Ω	L_{Tx} / μH	R_{Tx} / mΩ
ICN 1	sim.	pri.	6.21	200	12	25699	5.47	219	90.1	0.62	0.54	30.2	26.8		
		sec.	**16.3**	12.0	4 · 36										
	meas.	pri.	6.65	233	12	25699	6.08	**215**	90.8	0.63	0.57	**33.0**	32.6	14.4	17.2
		sec.	**16.7**	12.5	4 · 36										
ICN 2	sim.	pri.	6.88	200	13	26042	4.09	230	77.1	0.94	0.56	40.8	27.6		
		sec.	**7.73**	5.5	6 · 24										
	meas.	pri.	6.85	210	13	26042	4.39	**220**	76.4	0.94	0.60	**43.0**	31.1	9.74	10.9
		sec.	**7.8**	5.8	6 · 24										

This deviation from the optimum of $r_i/r_o = 5.3$ is a compromise to gain more space for a feasible winding through the center of the toroid, to reduce the number of inner layers, to increase the air cooling surface, and to comply with a limit on the available construction height. Basically, we calculated the optimal design to fully utilize the available construction space height h and then opted to increase r_i while keeping the other parameters constant.

Regarding the primary winding, a dense (localized) winding is unsuited due to a low k, as reasoned in Sec. III C 4. Sparse windings on a helical path yielded the best results, thereby forming a toroid on top of the outer surface around the L_2 toroid, as shown in Figs. 2(a), 2(b), and 7(a).

To minimize AC losses within the conducting material, a silk-wrapped litz wire of 2000 strands of 50 μm copper (effective copper cross section of 3.1 mm^2) is used for the secondary transformer winding. The primary winding consists of 400 strands of 50 μm copper (effective copper cross section of 0.78 mm^2) and is wrapped in a shrinking tube to increase durability and breakdown voltage. Parallel segments are connected on a 1 mm thick copper plate (top and bottom), which serves primarily as a distribution platform and connects parallel litz wires of the HCR and the ICN with a solder connection. In addition, balancing currents can be equalized on this low resistance copper plate.

C. Measurements

Measurements of inductors are performed with the LCR meter *Keysight* E4980AL (Keysight Technologies, CA, USA) at the channel's frequency. The coupling coefficient of a transformer is measured by using the short and open circuit inductances[63] in

$$k \approx \sqrt{1 - \frac{L_1|_{L_2\ \mathrm{short}}}{L_1|_{L_2\ \mathrm{open}}}}. \tag{18}$$

Note that L_2 needs to be sufficiently shorted (more difficult at high frequencies), and the quality factor of the secondary side should be $Q > 50$ for this model to be accurate. A comparison of different measurement techniques at higher leakage can be found in Ref. 64.

The LCR meter is used for Table I to determine L, the series resistance R, and k in the measured rows. All other values in these rows are calculated: M via (5), Q_{ICN} via (6) with L and R_2 of the same row, similarly Q_{HCR} with L and $R_s = R_2 + R_{\mathrm{Tx}}$, n via (3) using the primary and secondary measured L, and G via (7) for each row. For the simulated rows of Table I, L and M were obtained from the simulation in CONCEPT-II, and k was calculated via (5) here.

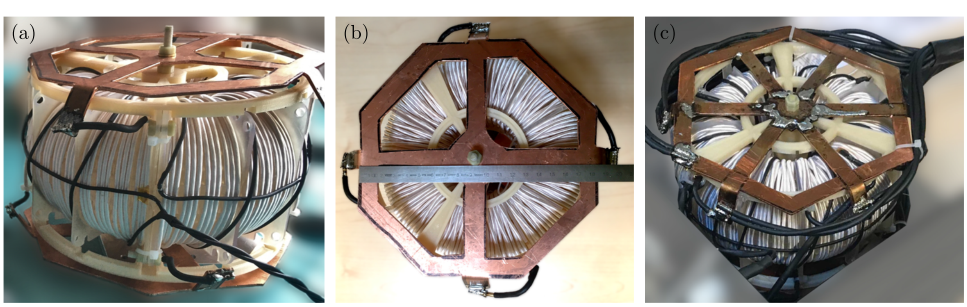

FIG. 7. Two ICNs for a two channel MPI system. In (a), the ICN 1 with $N_s = 4$ segments is shown (primary winding in black), and in (b), the top of the same ICN is shown with a reference scale in cm (without primary winding). ICN 2 with $N_s = 6$ segments is shown in (c) after installation. The connecting litz wire of the HCR and the primary winding are insulated with a black shrinking tube.

V. RESULTS

We have designed, simulated, and fabricated two ICNs with f_{r_1} = 25.699 kHz (N_s = 4) and f_{r_2} = 26.042 kHz (N_s = 6) for a two channel human-sized MPI system and integrated both into our MPI scanner.[11] The simulation and measurement results of the final design are summarized in Table I, and details of the construction are described in Sec. IV B. Pictures of both constructed ICNs are shown in Fig. 7.

The deviation between measured and simulated inductances L_2 is below 2.5% and below 1% for the first and second ICN, respectively. The measured value for k is about 5%–7% larger than the simulated value. Therefore, M is also larger in rows 2 and 4, because its calculation is based on k and L_2. This results in the measured G being 9.3% and 5.4% larger for ICN 1 and 2, respectively. Q_{ICN} refers only to the self-inductance L_2 and series R_2 of the secondary transformer side, while Q_{HCR} is the more important measure that includes the entire resonant load. Here, $R_s = R_2 + R_{\text{Tx}}$ represents the losses of the HCR and resembles the gain actually achieved. Later current measurements showed a gain very similar to these values, although they are marginally lower due to losses of additional connections and wires (e.g., decoupling capacitors).

The inductors of DFG and ICN are nearly matched for both channels, as explained in Sec. III D, with $L_{\text{Tx},1}$ = 14.4 μH ≈ $L_{2,1}$ = 16.7 μH for channel 1, and with $L_{\text{Tx},2}$ = 9.74 μH ≈ $L_{2,2}$ = 7.8 μH for channel 2. Note that the target input impedance Z_{prim} of (9) remains for both ICNs at around 30 Ω, which is the load after the bandpass filter. In addition, the Q of both ICNs remains constant, with 215 ≈ 220 (measured values) for the different segmentations, as argued in Sec. III C. The increase in G is achieved by the augmentation of n due to the segmentation.

Due to the non-orthogonal DFG channels, there is a residual coupling of $k = 0.062$,[11] which has serious implications for both resonators, as described in Sec. III E. The channels were decoupled by −35 dB using a single common decoupling capacitor carrying both currents $i_{r,1}$ and $i_{r,2}$. This choice provided good results with minimal changes to the existing HCR without introducing a large series resistance and with high temperature stability.

VI. DISCUSSION

Applications that require highly linear transformers, such as MPI, rely on circuits that do not utilize magnetic materials that saturate. Any harmonic distortion may obscure the weak receiving signal and degrade the image quality. As a result, air-core structures are chosen at the expense of increasing component dimensions, which sets the maximum Q for an available construction volume. In this study, we present a blueprint for a high-gain linear transformer with a high quality factor. We formulate an expression for the gain as a function of mutual inductance, optimize the cross-sectional shape, employ segmentation to shift the nominal inductance, deduce a primary winding topology, and incorporate multiple layers to enhance performance. In the context of the emerging imaging modality MPI, we establish a matching condition that balances particle signal and power consumption. Furthermore, we elaborate on various decoupling techniques for multichannel systems and support our assessment of the ICN with simulations.

In terms of human safety, the entire HCR has floating potentials, and component voltages in patient proximity are reduced by the ICN due to its high current gain that drives the low-inductance DFG to generate the required MPI drive-field. The symmetric design of the HCR allows for fundamental filtering at the signal tap but results in partial received signal attenuation due to the inductive voltage divider of L_2 and L_{Tx}. The TxRx topology generally reduces power consumption by saving space through the elimination of dedicated receive coils, but consumption is approximately doubled by the ICN. In addition, common decoupling strategies, such as gradiometric receive coils, reduce the design requirements for linearity within the transmit chain. A direct comparison in signal quality between this TxRx topology and a gradiometric receive topology is currently pending, although other TxRx systems have been characterized.[24]

The presented toroidal transformer blueprint is limited by its restriction to the quasi-static regime of electromagnetics, where wave propagation effects are not dominant. In addition, if AC losses due to proximity effects dominate in the toroid, the D-shape optimization will result in a different shape.[46] Parameters given or assumed in this study, such as frequency or volume, require careful selection. Q increases linearly with frequency and should be chosen as high as possible, taking into account component voltages, high reactive power (in resonance),[9] signal induction, wave propagation effects at high harmonics, required receive bandwidth, PNS, and SAR limits.[3,6,65–67] Our decision regarding the deviation of r_o/r_i from the optimum was aimed at facilitating the winding process and reducing the number of stacked inner layers. This decision allowed the winding of a nearly dense outer layer with two to three stacked inner layers. Regarding (10) with a given constant area and a linearly increasing r_c, we assume that the deviation from the optimal inductance is small. The copper plates at the top and bottom (nodes of parallel segments) should be designed to facilitate air cooling of the inner layers.

A key insight is that the available construction space should be exhausted, and the quality factor of the ICN benefits from a large volume, yielding a high gain. Therefore, the construction volume should be as large as cost, weight, and size factors will allow. If a lower L_2 is desired compared to a single winding on the maximized toroid, segmentation provides the means to reduce both inductance and resistance at the same rate with a constant Q. Note that this also increases the turns ratio n, causing a higher gain G. Independent of geometric choices, the method of moment based simulation provided accurate results, and the simulated inductance value deviated less than 2.5% from the manufactured ICNs. Two linear ICNs were built based on our presented schematic optimization that fed a floating two-channel HCR, including crosstalk decoupling, for a human-sized MPI head scanner[11] to fulfill safety precautions on a path toward the clinical integration of MPI.

SUPPLEMENTARY MATERIAL

An LTspice simulation (.asc) and a brief guide (.pdf) are provided in the supplementary material. The simulation includes a two-channel ICN transmit chain with and without coupling to investigate HCR behavior and decoupling performance. Its use and configuration are briefly explained in the guide document.

ACKNOWLEDGMENTS

We are very grateful to Christian Findeklee for discussions, proofreading, and initial input on variations of resonant circuit decoupling. The authors would also like to thank Heinz-D. Brüns and Christian Schuster of the Institut für Theoretische Elektrotechnik from the Hamburg University of Technology for providing the CONCEPT-II software and assisting with questions regarding simulations.

This work was supported by the German Research Foundation (DFG, Grant Nos. GR 5287/2-1 and KN 1108/7-1) and the Forschungszentrum Medizintechnik Hamburg (Grant No. 01fmthh2018). The Fraunhofer IMTE is supported by the EU (EFRE) and the State of Schleswig-Holstein, Germany (Project: IMTE, Grant No. 124 20 002/LPW-E1.1.1/1536). Publishing fees are supported by the Funding Program Open Access Publishing of Hamburg University of Technology (TUHH).

AUTHOR DECLARATIONS

Conflict of Interest

The authors have no conflicts to disclose.

Author Contributions

F.M., F.F., F.T., T.K., and M.G. contributed to the conceptualization and theory. F.M. and F.F. performed the simulations and measurements. F.M., F.F., F.T., and M.G. constructed the MPI components. I.S. contributed to the multichannel circuit analysis and decoupling theory. T.K. and M.G. supervised the project. F.M. wrote the original draft with support of M.M., M.G., F.F., F.T., I.S., and T.K. All authors reviewed the manuscript.

Fabian Mohn: Conceptualization (equal); Data curation (equal); Formal analysis (equal); Investigation (equal); Methodology (equal); Software (equal); Validation (equal); Visualization (equal); Writing – original draft (equal); Writing – review & editing (equal). **Fynn Förger**: Conceptualization (equal); Data curation (equal); Formal analysis (equal); Investigation (equal); Methodology (equal); Software (equal); Writing – review & editing (equal). **Florian Thieben**: Conceptualization (equal); Data curation (equal); Formal analysis (equal); Investigation (equal); Methodology (equal); Validation (equal); Writing – review & editing (equal). **Martin Möddel**: Formal analysis (equal); Investigation (equal); Writing – original draft (equal); Writing – review & editing (equal). **Ingo Schmale**: Conceptualization (equal); Investigation (equal); Validation (equal); Writing – review & editing (equal). **Tobias Knopp**: Conceptualization (equal); Funding acquisition (equal); Methodology (equal); Project administration (equal); Resources (equal); Supervision (equal); Writing – review & editing (equal). **Matthias Graeser**: Conceptualization (equal); Data curation (equal); Formal analysis (equal); Funding acquisition (equal); Investigation (equal); Methodology (equal); Project administration (equal); Supervision (equal); Validation (equal); Writing – original draft (equal); Writing – review & editing (equal).

DATA AVAILABILITY

The data that support the findings of this study are available from the corresponding author upon reasonable request.

APPENDIX: SLIGHTLY DETUNED RESONATORS

Let ω_1 and ω_2 be the channel frequencies of channel 1 and 2, respectively, and $\Delta\omega = \omega_1 - \omega_2$. Only ω_1 in channel 1 is excited and we approximate the impedance of the coupled second resonator for small $\Delta\omega$. $R_{s,2}$ is the real part of the resistance of channel 2 at resonance. The first order Taylor series expansion of the impedance of channel 2 yields

$$\begin{aligned} Z_2(\omega_2 + \Delta\omega) &= Z(\omega_2) + \Delta\omega \cdot \left.\frac{\mathrm{d}Z(\omega)}{\mathrm{d}\omega}\right|_{\omega_2} \\ &= R_{s,2} + \Delta\omega\, j\left(L + \frac{1}{\omega_2^2 C}\right) \\ &= R_{s,2} + j2\Delta\omega\, L. \end{aligned} \tag{A1}$$

We insert $L = \frac{1}{\omega_2^2 C}$ which is an expression of the resonance condition $\mathrm{Im}(Z_2) = 0$ at ω_2 for a RLC resonant circuit. Here, L is the sum of all inductances within the circuit. Consequently, we can rewrite (A1) into

$$\begin{aligned} Z_2(\omega_2 + \Delta\omega) &= R_{s,2}\left(1 + j2\frac{\Delta\omega}{\omega_2}\frac{\omega_2 L}{R_{s,2}}\right) \\ &= R_{s,2}\left(1 + j2\frac{\Delta\omega}{\omega_2} Q\right). \end{aligned} \tag{A2}$$

With a $\frac{\Delta\omega}{\omega_2}$ of $\frac{1}{75}$ and a $Q > 200$, we obtain a dominating imaginary part and the equation simplifies to $Z_2(\omega_2 + \Delta\omega) \approx j2\Delta\omega L$.

REFERENCES

[1] B. Gleich and J. Weizenecker, "Tomographic imaging using the nonlinear response of magnetic particles," Nature **435**, 1214–1217 (2005).
[2] P. C. Lauterbur, "Image formation by induced local interactions: Examples employing nuclear magnetic resonance," Nature **242**, 190–191 (1973).
[3] I. Schmale, B. Gleich, J. Rahmer, C. Bontus, J. Schmidt, and J. Borgert, "MPI safety in the view of MRI safety standards," IEEE Trans. Magn. **51**, 6502604 (2015).
[4] O. Dössel and J. Bohnert, "Safety considerations for magnetic fields of 10 mT to 100 mT amplitude in the frequency range of 10 kHz to 100 kHz for magnetic particle imaging," Biomed. Tech./Biomed. Eng. **58**, 611–621 (2013).
[5] B. Gleich, J. Weizenecker, and J. Borgert, "Experimental results on fast 2D-encoded magnetic particle imaging," Phys. Med. Biol. **53**, N81–N84 (2008).
[6] I. Schmale, B. Gleich, J. Schmidt, J. Rahmer, C. Bontus, R. Eckart, B. David, M. Heinrich, O. Mende, O. Woywode, J. Jokram, and J. Borgert, "Human PNS and SAR study in the frequency range from 24 to 162 kHz," in *2013 International Workshop on Magnetic Particle Imaging, IWMPI 2013* (IEEE, 2013), p. 1.
[7] I. N. Weinberg, P. Y. Stepanov, S. T. Fricke, R. Probst, M. Urdaneta, D. Warnow, H. Sanders, S. C. Glidden, A. McMillan, P. M. Starewicz, and J. P. Reilly, "Increasing the oscillation frequency of strong magnetic fields above 101 kHz significantly raises peripheral nerve excitation thresholds," Med. Phys. **39**, 2578–2583 (2012).
[8] Z. W. Tay, D. W. Hensley, P. Chandrasekharan, B. Zheng, and S. M. Conolly, "Optimization of drive parameters for resolution, sensitivity and safety in magnetic particle imaging," IEEE Trans. Med. Imaging **39**, 1724–1734 (2020).

[9] I. Schmale, B. Gleich, O. Mende, and J. Borgert, "On the design of human-size MPI drive-field generators using RF litz wires," in *2015 5th International Workshop on Magnetic Particle Imaging (IWMPI)* (IEEE, Istanbul, Turkey, 2015), p. 1.
[10] T. F. Sattel, O. Woywode, J. Weizenecker, J. Rahmer, B. Gleich, and J. Borgert, "Setup and validation of an MPI signal chain for a drive field frequency of 150 kHz," IEEE Trans. Magn. **51**, 6501703 (2015).
[11] F. Thieben, F. Foerger, F. Mohn, N. Hackelberg, M. Boberg, J.-P. Scheel, M. Möddel, M. Graeser, and T. Knopp, "System characterization of a human-sized 3D real-time magnetic particle imaging scanner for cerebral applications," Commun Eng **3**, 47 (2024).
[12] Z. W. Tay, D. Hensley, J. Ma, P. Chandrasekharan, B. Zheng, P. Goodwill, and S. Conolly, "Pulsed excitation in magnetic particle imaging," IEEE Trans. Med. Imaging **38**, 2389–2399 (2019).
[13] F. Mohn, T. Knopp, M. Boberg, F. Thieben, P. Szwargulski, and M. Graeser, "System matrix based reconstruction for pulsed sequences in magnetic particle imaging," IEEE Trans. Med. Imaging **41**, 1862 (2022).
[14] S. Valtchev, E. Baikova, and L. Jorge, "Electromagnetic field as the wireless transporter of energy," Facta Univ., Ser.:Electron. Energ. **25**, 171–181 (2012).
[15] S. Morita, T. Hirata, E. Setiawan, and I. Hodaka, "Power efficiency improvement of wireless power transfer using magnetic material," in *2017 2nd International Conference on Frontiers of Sensors Technologies (ICFST)* (IEEE, Shenzhen, 2017), pp. 304–307.
[16] S. A. Mirbozorgi, H. Bahrami, M. Sawan, and B. Gosselin, "A smart multicoil inductively coupled array for wireless power transmission," IEEE Trans. Ind. Electron. **61**, 6061–6070 (2014).
[17] J. Yang, Y. Shi, W. Y. Wei, and H. Shen, "A wireless power transfer system based on impedance matching network," Int. J. RF Microwave Comput.-Aided Eng. **30**, e22437 (2020).
[18] Z. Tong, W. D. Braun, and J. M. Rivas-Davila, "3-D printed air-core toroidal transformer for high-frequency power conversion," in *2019 20th Workshop on Control and Modeling for Power Electronics (COMPEL)* (IEEE, Toronto, ON, Canada, 2019), pp. 1–7.
[19] P. Ziegler, J. Haarer, J. Ruthardt, M. Nitzsche, and J. Roth-Stielow, "Air-core toroidal transformer concept for high-frequency power converters," in *PCIM Europe Digital Days 2020; International Exhibition and Conference for Power Electronics, Intelligent Motion, Renewable Energy and Energy Management* (IEEE, 2020), pp. 1–5.
[20] J. Stelzner, G. Bringout, M. Graeser, and T. M. Buzug, "Toroidal variometer for a magnetic particle imaging device," in *International Workshop on Magnetic Particle Imaging (IWMPI)* (IEEE Xplore Digital Library, 2015), p. 1.
[21] K. Bernacki, D. Wybrańczyk, M. Zygmanowski, A. Latko, J. Michalak, and Z. Rymarski, "Disturbance and signal filter for power line communication," Electronics **8**, 378 (2019).
[22] B. Wang and Z. Cao, "Design of active power filter for narrow-band power line communications," MATEC Web Conf. **189**, 04012 (2018).
[23] E. Mattingly, E. Mason, M. Sliwiak, and L. L. Wald, "Drive and receive coil design for a human-scale MPI system," Int. J. Magn. Part. Imaging **8**(1), (published online, 2022).
[24] H. Paysen, O. Kosch, J. Wells, N. Loewa, and F. Wiekhorst, "Characterization of noise and background signals in a magnetic particle imaging system," Phys. Med. Biol. **65**, 235031 (2020).
[25] W. R. Johnson, "Filtering techniques for noise suppression in quasi-balanced circuits," Technical Report No. 32-945, Jet Propulsion Laboratory, 1966.
[26] P. Vogel, M. A. Rückert, C. Greiner, J. Günther, T. Reichl, T. Kampf, T. A. Bley, V. C. Behr, and S. Herz, "iMPI: Portable human-sized magnetic particle imaging scanner for real-time endovascular interventions," Sci. Rep. **13**, 10472 (2023).
[27] J. Borgert, J. D. Schmidt, I. Schmale, C. Bontus, B. Gleich, B. David, J. Weizenecker, J. Jockram, C. Lauruschkat, O. Mende, M. Heinrich, A. Halkola, J. Bergmann, O. Woywode, and J. Rahmer, "Perspectives on clinical magnetic particle imaging," Biomed. Tech./Biomed.Eng. **58**, 551–556 (2013).
[28] M. Graeser, T. Knopp, M. Grüttner, T. F. Sattel, and T. M. Buzug, "Analog receive signal processing for magnetic particle imaging," Med. Phys. **40**, 042303 (2013).
[29] M. Graeser, T. Knopp, P. Szwargulski, T. Friedrich, A. Von Gladiss, M. Kaul, K. M. Krishnan, H. Ittrich, G. Adam, and T. M. Buzug, "Towards picogram detection of superparamagnetic iron-oxide particles using a gradiometric receive coil," Sci. Rep. **7**, 6872 (2017).
[30] H. Radermacher, F. Schrank, D. Pantke, F. Mueller, M. Peters, and V. Schulz, "Highly flexible gradiometer coil arrangement offering improved passive compensation for multi-frequency MPI," Int. J. Magn. Part. Imaging **9**(1), (published online, 2023).
[31] C. McDonough, J. Pagan, and A. Tonyushkin, "Implementation of the surface gradiometer receive coils for the improved detection limit and sensitivity in the single-sided MPI scanner," Phys. Med. Biol. **67**, 245009 (2022).
[32] H. Paysen, J. Wells, O. Kosch, U. Steinhoff, J. Franke, L. Trahms, T. Schaeffter, and F. Wiekhorst, "Improved sensitivity and limit-of-detection using a receive-only coil in magnetic particle imaging," Phys. Med. Biol. **63**, 13NT02 (2018).
[33] J. Weizenecker, B. Gleich, J. Rahmer, H. Dahnke, and J. Borgert, "Three-dimensional real-time *in vivo* magnetic particle imaging," Phys. Med. Biol. **54**, L1–L10 (2009).
[34] Institut für Theoretische Elektrotechnik, *CONCEPT-II v12.0, TET*, 2023.
[35] A. A. Ozaslan, A. R. Cagil, M. Graeser, T. Knopp, and E. U. Saritas, "Design of a magnetostimulation head coil with Rutherford cable winding," Int. J. Magn. Part. Imaging **6**(2), (published online, 2020).
[36] Y. Zhaksylyk, E. Halvorsen, U. Hanke, and M. Azadmehr, "Analysis of fundamental differences between capacitive and inductive impedance matching for inductive wireless power transfer," Electronics **9**, 476 (2020).
[37] I. Daut, S. Hasan, S. Taib, R. Chan, and M. Irwanto, "Harmonic content as the indicator of transformer core saturation," in *2010 4th International Power Engineering and Optimization Conference (PEOCO)* (IEEE, Shah Alam, Selangor, Malaysia, 2010), pp. 382–385.
[38] J. Ramírez-Niño, C. Haro-Hernández, J. H. Rodriguez-Rodriguez, and R. Mijarez, "Core saturation effects of geomagnetic induced currents in power transformers," J. Appl. Res. Technol. **14**, 87–92 (2016).
[39] D. Shmilovitz, "On the definition of total harmonic distortion and its effect on measurement interpretation," IEEE Trans. Power Delivery **20**, 526–528 (2005).
[40] AETechron, "Datasheet: AE Techron 7136 high-speed AC/DC amplifier," AE Techron 7136, 2023.
[41] AETechron, "Datasheet: AE Techron 7224 gradient power amplifier," AE Techron 7224, 2023.
[42] Crown, "Datasheet: XLi series operation manual," Crown Audio by Harman, 2023.
[43] Dr. Hubert, "Datasheet: 4-quadrant precision amplifier A1110-40-QE," Dr. Hubert GmbH, 2023.
[44] I. Micrometals, "Datasheet: Power conversion and line filter applications," Micrometals Powder Core Solutions, 2007.
[45] D. Herceg, K. Chwastek, and D. Herceg, "The use of hypergeometric functions in hysteresis modeling," Energies **13**, 6500 (2020).
[46] P. N. Murgatroyd, "Some optimum shapes for toroidal inductors," IEE Proc. B **129**, 168–176 (1982).
[47] C. Sullivan, "Optimal choice for number of strands in a litz-wire transformer winding," IEEE Trans. Power Electron. **14**, 283–291 (1999).
[48] R. R. Mett, J. W. Sidabras, and J. S. Hyde, "MRI surface-coil pair with strong inductive coupling," Rev. Sci. Instrum. **87**, 124704 (2016).
[49] A. Ayachit and M. K. Kazimierczuk, "Transfer functions of a transformer at different values of coupling coefficient," IET Circuits Devices Syst. **10**, 337–348 (2016).
[50] A. Witulski, "Introduction to modeling of transformers and coupled inductors," IEEE Trans. Power Electron. **10**, 349–357 (1995).
[51] P. Zacharias, *Magnetic Components: Basics and Applications* (Springer Fachmedien Wiesbaden, Wiesbaden, 2022).
[52] A. Zolfaghari, A. Chan, and B. Razavi, "Stacked inductors and transformers in CMOS technology," IEEE J. Solid-State Circuits **36**, 620–628 (2001).

[53] P. Murgatroyd, "The optimal form for coreless inductors," IEEE Trans. Magn. **25**, 2670–2677 (1989).
[54] P. N. Murgatroyd and D. Belahrache, "Economic designs for single-layer toroidal inductors," IEEE Proc. B **132**, 315 (1985).
[55] P. N. Murgatroyd and D. P. Eastaugh, "Optimum shapes for multilayered toroidal inductors," IEEE Proc. **147**, 75 (2000).
[56] P. D. Evans and W. J. B. Heffernan, "Power transformers and coupled inductors with optimum interleaving of windings," Patent EP0547120B1, 1990.
[57] V. D. Shafranov, "Optimum shape of a toroidal solenoid," Sov. Phys.-Tech. Phys. **17**(9), 1433–1437 (1973) (Engl. Transl.).
[58] W. Rogowski and W. Steinhaus, "Die Messung der magnetischen Spannung: Messung des Linienintegrals der magnetischen Feldstärke," Arch. Elektrotech. **1**, 141–150 (1912).
[59] T. Knopp, N. Gdaniec, and M. Möddel, "Magnetic particle imaging: From proof of principle to preclinical applications," Phys. Med. Biol. **62**, R124–R178 (2017).
[60] A. von Gladiss, M. Graeser, and T. M. Buzug, "Influence of excitation signal coupling on reconstructed images in magnetic particle imaging," in *Informatik Aktuell*, edited by A. Maier, T. M. Deserno, H. Handels, K. H. Maier-Hein, C. Palm, and T. Tolxdorff (Springer, Berlin, Heidelberg, 2018), Vol. 211279, pp. 92–97.
[61] Analog Devices Inc., *LTspice v17.1.10*, ADI, 2023.
[62] W. C. Gibson, *The Method of Moments in Electromagnetics* (Chapman and Hall/CRC, Boca Raton, 2008).
[63] MIT Department of Electrical Engineering, *Magnetic Circuits and Transformers: A First Course for Power and Communication Engineers* (The MIT Press, 1977).
[64] J. Hayes, N. O'Donovan, M. Egan, and T. O'Donnell, "Inductance characterization of high-leakage transformers," in *Eighteenth Annual IEEE Applied Power Electronics Conference and Exposition, 2003. APEC'03* (IEEE, Miami Beach, FL, USA, 2003), Vol. 2, pp. 1150–1156.
[65] J. Bohnert and O. Dössel, "Effects of time varying currents and magnetic fields in the frequency range of 1 kHz to 1 MHz to the human body—A simulation study," in *2010 Annual International Conference of the IEEE Engineering in Medicine and Biology* (IEEE, Buenos Aires, 2010), pp. 6805–6808.
[66] E. U. Saritas, P. W. Goodwill, G. Z. Zhang, and S. M. Conolly, "Magnetostimulation limits in magnetic particle imaging," IEEE Trans. Med. Imaging **32**, 1600–1610 (2013).
[67] D. Grau-Ruiz, J. P. Rigla, E. Pallás, J. M. Algarín, J. Borreguero, R. Bosch, G. López-Comazzi, F. Galve, E. Díaz-Caballero, C. Gramage, J. M. González, R. Pellicer, A. Ríos, J. M. Benlloch, and J. Alonso, "Magneto-stimulation limits in medical imaging applications with rapid field dynamics," Phys. Med. Biol. **67**, 045016 (2022).